Characterization of atmospheric aerosol optical properties based on the combined use of a ground-based Raman lidar and an airborne optical particle counter in the framework of the Hydrological Cycle in the Mediterranean Experiment – Special Observation Period 1

5

Dario Stelitano[1,2], Paolo Di Girolamo[1], Andrea Scoccione[3], Donato Summa[2], Marco Cacciani[3]

[1] Scuola di Ingegneria, Università degli Studi della Basilicata, 85100 Potenza – Italy
[2] now at Osservatorio Nazionale Terremoti, Istituto Nazionale di Geofisica e Vulcanologia, 00143 Roma – Italy
[3] Dipartimento di Fisica, Università di Roma "La Sapienza", Piazzale Aldo Moro, n. 2, 00100 Roma – Italy

10   *Correspondence to*: Paolo Di Girolamo (paolo.digirolamo@unibas.it)

Abstract. Vertical profiles of particle backscattering coefficient at 355, 532 and 1064 nm measured by the lidar Raman system BASIL have been compared with simulated particle backscatter profiles obtained through a Mie scattering code based on the use of simultaneous and almost co-located profiles provided by an air-borne optical particle counter. . Measurements were carried out during dedicated flights of the French research aircraft ATR42 in the frame of the European

15   Facility for Airborne Research (EUFAR) Project "WaLiTemp", as part of the Hydrological Cycle in the Mediterranean Experiment - Special Observation Period 1 (HyMeX-SOP1). Results from two selected case studies are reported and discussed in the paper and two slightly different analysis approaches are illustrated and applied to the dataset. Results reveal a good agreement between measured and simulated multi-wavelength particle backscattering profiles. Specifically, simulated and measured particle backscattering profiles at 355 and 532 nm are found to deviate less than 15 % (mean value=7 %) and

20   50 % (mean value=30%), respectively, when considering the presence of a Continental/Urban aerosol component. Reported results reveal a good agreement between measured and simulated multi-wavelength particle backscatter profiles, which ultimately testifies lidar ability to infer the aerosol type from these measurements.

1 Introduction

Aerosols are a key atmospheric component, playing a major role in meteo-climatic processes. Aerosols influence

25   precipitation processes and the water cycles primary through two effects: the direct effect, as a result of the interaction in the form of scattering with solar radiation (among others, Haywood and Boucher, 2000; Takemura et al., 2005), and the indirect effect, as a result of the interaction with clouds (among others, Sekiguchi et al., 2003; Yang et al., 2011). A semi-direct effect can also arise in the presence of high aerosol loading, determining a scattering and absorption enhancement, ultimately leading to an alteration of the atmospheric stability conditions (e.g. Mitchell, 1971). Despite aerosol well-recognized

Atmospheric
Measurement
Techniques
Discussions

30   importance in meteorological and climate studies, only a limited number of remote sensing techniques can provide vertically resolved measurements of the microphysical properties of this important atmospheric component. For example, in-situ sensors transported by air balloons or any other flying vector allow measuring the vertical profile of aerosol size and microphysical properties, with high vertical resolution (of the order of 10 m), but typically with a limited temporal resolution. Any experiment aimed at characterizing the temporal evolution of aerosol microphysical properties would require

35   several consecutive balloon launches or flights, with the time lag between two consecutive launches/flights unlikely being smaller than 1 hour, with consequent detriment of the temporal resolution. Additionally, in-situ particle sensors are quite heavy and bulky, which - in the case of balloon-borne experiments - implies the use of quite large aerostatic balloons. This makes monitoring very expensive and logistically difficult to implement.

Remote sensing techniques can overcome these limitations. A variety of passive optical remote sensors (i.e. spectro-
40   radiometers, sun and sky photometers, etc.) have demonstrated their capability to characterize aerosol microphysical properties, but they lack in vertical resolution, which makes them scarcely suited for vertically resolved measurements of aerosol size and microphysical properties. Low vertical resolution is combined with a limited temporal resolution when these techniques are implemented sun-synchronous orbiting platforms, with a typical "revisit time" of several hours. Active remote sensing systems may overcome this limitation. Specifically, lidar systems with aerosol measurement capability are

45   characterized by high accuracies and temporal/vertical resolutions, which makes them particularly suited for this kind of applications. Lidar measurements of aerosol optical properties have been reported since the early sixties (among others, Fiocco and Grams, 1964; Elterman, 1966). Originally, measurements were carried out with single-wavelength elastic backscatter lidars capable to provide vertical profiles of the particle backscattering coefficient at the laser wavelength. In these systems the particle backscattering coefficient is determined from the elastic lidar signals based on the application of

50   the Klett-Fernald-Sasano approach (Klett, 1981, 1985; Fernald, 1984). More recently, the acquired capability to measure roto-vibrational Raman lidar signals from nitrogen and oxygen molecules has made the determination of the particle extinction coefficient also possible (Ansmann, 1990; 1992). The possibility to retrieve particle size and microphysical parameters from multi-wavelength lidar data of particle backscattering, extinction and depolarization has been recently demonstrated by a variety of authors (Müller et al., 2001, 2007, 2009; Veselovskii et al., 2002, 2009, 2010). This

55   measurement capability can be combined with the capability to measure atmospheric thermodynamic profiles (Wulfmeyer et al., 2005; Di Girolamo et al., 2008, 2018a) to characterize aerosol-cloud interaction mechanisms. The ground-based University of Basilicata Raman Lidar system (BASIL) has a demonstrated capability to provide high-quality and accurate multi-wavelength Raman lidar measurements for the retrieval of particle size and microphysical parameters (Veselovskii et al., 2010; Di Girolamo et al., 2012). The system was deployed in Candillargues (Southern France) in the period August-

60   November 2012, in the frame of the Hydrological cycle in the Mediterranean Experiment (HyMeX) Special Observation Period 1 (SOP1). In the present manuscript, measurements collected by BASIL are illustrated with the purpose to characterize atmospheric aerosol optical properties. These measurements, in combination with in-situ measurements from an airborne optical particle counter and the application of a Mie scattering code, are used to infer aerosol types and their

Atmospheric
Measurement
Techniques
Discussions

primary microphysical properties. The outline of the paper is the following: section 2 is dedicated to the description of the

65   Raman lidar system BASIL and the airborne optical particle counter; section 3 illustrates HyMeX-SOP1. The methodology
is illustrated in section 4, while measurements and simulations are reported in section 5. Finally, section 6 summarizes all
results and provides some indications for possible future activities.

2 Instrumental setup

2.1 BASIL

70   The Raman lidar BASIL was built around a pulsed Nd:YAG laser, emitting pulses at 355, 532 and 1064 nm, with a
repetition rate of 20 Hz. The system includes a large telescope in Newtonian configuration, with a 400 mm diameter primary
mirror, primarily used to collect Raman and higher range signals. Two additional smaller telescopes, developed around two
50 mm-diameter 200 mm-focal length lenses, are used to collect backscatter echoes at 1064 nm and total and cross-polarized
backscatter echoes at 532 nm. Laser emission at 355 nm (average power of 10 W) is used to stimulate Raman scattering from

75   water vapour, nitrogen and oxygen molecules (Di Girolamo et al., 2004, 2006, 2009a), which are ultimately used to measure
the vertical profiles of atmospheric temperature, water vapour mixing ratio and aerosol extinction coefficient. Elastic
scattering from aerosol and molecular species at 355, 532 and 1064 nm are used to measure the vertical profiles of the
aerosol backscattering coefficient at these three wavelengths. Raman echoes are very weak and degraded by solar radiation
in daytime. Consequently, the above specified high laser power and large telescope aperture are required to generate and

80   collect daytime Raman signals with a sufficient signal-to-noise ratio throughout a large portion of the troposphere. The
instrumental setup of BASIL has been described in detail in several papers (Di Girolamo et al., 2009a, 2009b, 2012a, 2012b;
2016; 2017; Bhawar et al., 2011).

2.2   Optical Particles Counter

An optical particle counter (OPC), manufactured by GRIMM Aerosol Technik GmbH (model Sky-OPC 1.129), is used to

85   measure the size resolved particle number concentration in the size range 0.25 - 32 μm. The sensor includes 31size bins. A
laser beam generated by a 683 nm diode laser invests aerosol particles exiting a pump chamber; the scattered radiation is
deflected by two separate mirrors and detected by the photo sensor (Heim et al., 2008). By summing up the particle number
over all sizes, the total number concentration is derived (Grimm and Eatough, 2009). The model used in the present effort
has a specific airborne design (McMeeking et al., 2010). The use of a differential pressure sensor and an external pump

90   allows the OPC measurements independently of environmental pressure conditions. The OPC was installed on-board the
French research aircraft ATR42, operated by the Service des Avions Instrumentés pour la Recherche en Environnement
(SAFIRE), as part of an ensemble of in-situ sensors for the characterization of aerosol and cloud size and microphysical
properties. Dedicated flights by the ATR42 were performed during HyMeX-SOP 1 in the frame of the Wa-Li-Temp EUFAR
project, with the aircraft looping up and down in the area of the Raman lidar system.

Atmospheric
Measurement
Techniques
Open Access
Discussions
EGU

3 HyMeX and the Special Observation Period 1

95

The Hydrological cycle in Mediterranean Experiment was conceived with the overarching goal of collecting a large set of atmospheric and oceanic data allowing for a better understanding of the hydrological cycle in the Mediterranean area. Within this experiment a major field campaign, the Special Observation Period 1 (SOP1), took place over the northwestern Mediterranean area in the period September–November 2012. During HyMeX-SOP1 the Raman lidar system BASIL was

100   deployed in the Cévennes-Vivarais atmospheric 'supersite', located in Candillargues (43^{0}37' N, 4^{0}04' E, elevation: 1m). BASIL was operated from 5 September to 5 November 2012, collecting more than 600 h of measurements, distributed over 51 measurement days and 19 Intensive Observation Periods (IOPs).

The French research aircraft ATR42, hosting the OPC, was stationed at Montpellier airport. Its main payload consisted of the airborne DIAL LEANDRE 2, profiling water vapour mixing ratio beneath the aircraft. The ATR42 payload also included in-

105   situ sensors for turbulence measurements, as well as aerosol/cloud microphysics probes. Among these, the OPC. During HyMeX-SOP1, the ATR42 performed more than 60 flight hours: 8 were supported by the EUFAR project "WaLiTemp" and the remaining were supported by the "Mediterranean Integrated STudies at Regional and Local Scales" (MISTRALS) Program. A specific flight pattern was defined for the purposes of the "WaLiTemp" project (figure 1), with the aircraft making spirals (hippodromes) up and down around a central location, originally aimed to be the atmospheric supersite in

110   Candillargues. Unfortunately, because of air-traffic restrictions, aircraft sensors' operation was typically started 30 km eastward. Flights hours in the frame of the "WALiTemp" project were carried out on 13 September, 02 and 29 October and 05 November 2012.

Spiral ascents and descents were carried out with a vertical speed of 150 m/min. During each flight, except in presence of specific logistic issues, a minimum of two ascent-descent spirals were carried out. For the purposes of the present

115   comparisons, in order to minimize effect associated with the sounding of different air masses, we selected days characterized by horizontally homogeneous atmospheric conditions.

4 Methodology

The volume scattering coefficient can be expressed as:

$$\beta_{\lambda_0}^{par} = \int_0^\infty Q_{back}(r) n(r) \, \mathrm{d}r \tag{1}$$

120   with $Q_{back}(r)$ being the particle scattering efficiency and $n(r)$ being the particle size distribution.

$Q_{back}(r)$ can be expressed as (Grainger *et al.*, 2004):

$$Q_{back} = \frac{2}{x^2} \sum_{n=1}^\infty (2n+1)\left(|a_n|^2 + |b_n|^2\right) \tag{2}$$

Atmospheric
Measurement
Techniques
Open Access
EGU
Discussions

where the terms a_n and b_n are the Mie scattering amplitudes of nth magnetic partial wave, which are obtained through the expressions:

$$a_n = \frac{\psi_n(x)\psi_n'(mx) - m\,\psi_n'(x)\psi_n(mx)}{\xi_n^{(1)}(x)\psi_n'(mx) - m\,\xi_n^{(1)'}(x)\psi_n(mx)} \qquad (3)$$

$$b_n = \frac{\psi_n'(x)\psi_n(mx) - m\,\psi_n(x)\psi_n'(mx)}{\xi_n^{(1)'}(x)\psi_n(mx) - m\,\xi_n^{(1)}(x)\psi_n'(mx)} \qquad (4)$$

where m is the complex refractive index; $x = 2\pi r / \lambda$ is the size parameter, given λ is the wavelength of the radiation and r is the radius of the sphere. The functions $\psi_n(x)$ and $\xi_n^{(1)}$ are Riccati–Bessel functions defined in terms of the spherical Bessel function of the first kind. A log-normal size distribution is considered in this study, with an analytical expression for each mode of the form (Grainger *et al.*, 2004):

$$n(r) = \frac{N_0}{\sqrt{2\pi}} \frac{1}{\ln S} \frac{1}{r} \exp\left[-\frac{(\ln r - \ln r_m)}{2\ln^2 S} \right] \qquad (5)$$

where r_m is the median radius of the distribution and the standard deviation of $\ln r$ is $\ln S$. Thus, the log-normal distribution is completely described by N_0, r_m and S. Specifically, particle concentration N_0 is obtained by minimizing the differences between the simulated size distribution and the one measured by the OPC, while the values of r_m and S are those identified in the following section based on literature results. Simulated backscatter profiles $\beta_{\lambda_0}^{par}(z)$ are the obtained through the application expression (1) at all altitudes covered by the OPC, considering the different refractive index and size parameters' values, which depend on the aerosol type, and integrating the expression over the three distribution modes. To perform these computations a specific scattering code was developed by the authors in IDL environment.

5 Results

5.1 Case Study on 13 September 2012

During the first ascending spiral, in-situ sensors on board the ATR42 were operated in the altitude region from 650 m to 5700 m above sea level (hereafter in the paper all altitudes are intended above sea level), covering the 40 min-time interval between 19.55 and 20.35 UTC. BASIL was operated in the time interval 19.00-23.00 UTC. Figure 2 illustrates the temporal evolution of the particle backscattering coefficient at 532 nm over the time interval 19.30-21.30 UTC. The figure is illustrated as a succession of 5 min vertical profiles with a vertical resolution of 7,5 m. The figure reveals the presence of a shallow nocturnal boundary layer, testified by the presence of an aerosol layer extending up to 500-600 m, and the presence of a residual layer extending up to 1500-2100 m.

Wind direction measurements performed by the on-board flight sensors reveal a primarily Northerly wind, with direction varying in the range ±30° depending on altitude. The NOAA HYSPLIT model (Draxler e Rolph, 1998; Stein et al., 2015) has been used to determine the origin of the sounded air-masses. The HYSPLIT model allows computing air parcel trajectories,

Atmospheric
Measurement
Techniques
Discussions

but it can also be used to simulate complex transport, dispersion, chemical transformation and deposition. A common application of the HYSPLIT model is the back- and forward- trajectory analysis, which is used to determine the origin or destination of air masses and establish source-receptor relationships.

155   In the present effort the HYSPLIT model is used to estimate air mass trajectories at specific altitude levels in the days preceding their arrival on the lidar site in Candillargues. Specifically, figure 3 illustrates the 5-days back-trajectories at 428 m (red line), 2828 m (blue line) and 5826 m (green line) of the air masses reaching the lidar site at 20 UTC on 13 September 2012.

Air masses reaching the measurement site at altitudes of 428 and 2828 m were originated around Iceland and Greenland and passed at low altitudes (< 400 m) over the North Atlantic Sea and over industrialized areas in France, while air masses at

160   5826 m originated in the North Atlantic Sea in the proximity of the Canadian coasts and persisted in marine environment for almost 5 days before reaching France. Based on the involved air masses, we formulate the hypothesis that low level sounded particles consist of continental polluted aerosols, while particles at higher altitudes are an internal mixture of continental polluted aerosols with marine salt (i.e. an aerosol coming from a marine polluted environment).

In order to properly model these different particle types, we speculate that aerosols transported from a continental area with

165   high anthropic impact are characterized by the presence of soot in nuclei mode, water soluble in accumulation mode and dust-like in coarse mode (d'Almeida et al., 1991). d'Almeida et al. (1991), Junge and Jaenicke (1971) and Junge (1972) suggested the use of a tri-modal log-normal size distribution (see expression 1 below), indicating specific values for the two primary size distribution parameters, i.e. the modal radius, $\bar{r}$, and standard deviation, σ: Specifically, d'Almeida et al. (1991), reported values of $\bar{r}$ and σ for the soot mode of 0.012 μm and 2.00, respectively, for the water soluble mode of 0.024

170   μm and 2.24, respectively, and for the dust-like mode 0.471 μm and 2.51, respectively. These values are considered in the following computations.

The log-normal size distribution has been computed considering the OPC data in the dimensional range 0.25 - 2.5 μm, with a 300 m vertical integration window. Results are illustrated in figure 4 (bold black line). In this same figure the size distribution was computed with the OPC data is compared with the theoretical distributions for the three different modes

175   (fine mode - red line, accumulation mode - violet line, coarse mode - light blue line).

For each of the three modes, the number of particles has been varied in order to have the total theoretical distribution (thin black line) matching the experimental distribution computed with the OPC data. The matching between the experimental and theoretical distributions has been optimized based on the application of a best fit procedure. This approach was applied to each altitude level. In figure 4, we are considering experimental and theoretical distributions at an altitude of 1529 m, this

180   being the lowest altitude where the OPC measured aerosols larger than 0.7 – 0.8 μm. Above 1529 m, the aerosol composition of the coarse mode has been modified by replacing the dust-like component with sea salt, consistently with the initial hypothesis of a different aerosol origin and composition above a definite altitude. The modal radius and distribution width ($\bar{r}$=0.3 μm and σ = 2.51, respectively) used in the simulations for this aerosol typology are again derived from literature (d'Almeida et al., 1991; Shettle and Fenn, 1976, 1979).

Atmospheric
Measurement
Techniques
Discussions

185   For the purpose of these simulations, values of the real, nr, and imaginary part, ni, of refractive index in the proximity of the
      three lidar wavelengths (355, 532 and 1064 nm) for the three different aerosol components are taken from different literature
      papers (d'Almeida et al., 1991; Shettle and Fenn, 1976; Shettle and Fenn, 1979; WCP–112, (986). These values are reported
      in Table 1.
      The vertical profiles of particle backscattering coefficient at 355, 532 and 1064 nm have been simulated through the above
190   specified Mie scattering code from the OPC data, considering values of $\bar{r}$ and σ for the different aerosol components.
      Figure 5 compares the vertical profiles of the measured (black line) and simulated (red line) particle backscattering
      coefficient at 355 nm. The measured profile is obtained from BASIL data integrated over the 40 min time interval coincident
      with the airplane ascent time (19.55-20.35 UTC on 13 September 2012), considering a vertical resolution of 300 m. The
      agreement between measured and simulated profiles appear quite good up to 4000 m.
195   Figure 6 compares the vertical profiles of measured (black line) and simulated (red line) particle backscattering coefficient at
      532 nm over the same 40 min time interval (19.55-20.35 UTC) on 13 September 2012, with a vertical resolution of 300 m.
      Lidar data at 532 nm are affected by a larger statistical uncertainty than the data at 355 nm. Also in this case, the agreement
      between measured and simulated profiles appear quite good up to 3500-4000 m.
      Figure 7 compares the vertical profiles of measured and simulated particle backscattering coefficient at 1064 nm over the
200   same 40 min time interval considered in figures 5 and 6, again with a vertical resolution of 300 m. Particle backscatter
      measurements at 1064 nm are affected by a statistical uncertainty larger than one affecting the data 532 nm. This large
      uncertainty is the result of the use of a reduced laser emission power at 1064 nm because of the restrictions imposed by the
      air traffic control authorities. In this case, the agreement between measured and simulated profiles is smaller, but still
      acceptable up to 3000 m.
205   In order to quantify the agreement between measured and simulated particle backscatter profiles at the three considered
      wavelengths, deviations for each profile pair expressed in terms of the root mean squared (RMS) deviation and BIAS were
      calculated using the following expressions (Behrendt et al., 2007; Bhawar et al., 2011):

$$BIAS_{i,relativo}(z_1, z_2) = \frac{2 \sum_{z=z_1}^{z_2} \{q_1(z) - q_2(z)\}}{\sum_{z=z_1}^{z_2} \{q_1(z) + q_2(z)\}} ,$$ (6)

$$RMS_{i,relativo}(z_1, z_2) = \frac{2 \sqrt{N_z \sum_{z=z_1}^{z_2} \{q_1(z) - q_2(z)\}^2}}{\sum_{z=z_1}^{z_2} \{q_1(z) + q_2(z)\}} ,$$ (7)

210   where $q_1(z)$ and $q_2(z)$ are the measured and simulated particle backscattering coefficient profile, respectively. It is to be
      pointed out that the BIAS quantifies the potential offset between the two profiles, while the root mean squared deviation
      includes all the possible deviations between the two profiles, which may be caused by systematic and statistical error sources
      affecting measured and simulated profiles, but may be also associated with atmospheric variability (i.e. different air masses
      sounded by BASIL and the OPC). Figure 8 shows the BIAS (left panel) and RMS deviation (right panel) profiles of the
215   measured vs. the simulated particle backscattering coefficient at 355 nm. Black and red lines represent two different
      variability ranges (± 10 % and ± 60 %, respectively, for BIAS, and 0-10 % and 0-100 % for RMS deviation, respectively).

The red and black scales are used to highlight the variability of these parameters at different altitudes. BIAS values are within the interval -1.3 ÷ 6.45 % up to 3900 m and exceed 25 % above this altitude; RMS deviation values are within the interval 1.2-7.5 % up to 3900 m, being as large as 28 % above this altitude.

220 Figure 9 shows the BIAS and RMS deviation profiles of the measured vs. the simulated particle backscattering coefficient at 532 nm. BIAS values are within ± 10 % up to 3000 m and RMS deviation values are not exceeding 15 % up to this same altitude. Finally, figure 10 shows the BIAS and RMS deviation profiles of the measured vs. the simulated particle backscattering coefficient at 1064 nm, with values for the former quantity within ± 30 % up to 2500 m and for the latter quantity smaller than 50 % up to this same altitude. Again, these large BIAS and RMS deviation values are the result of the

225 large statistical uncertainty affecting lidar measurements at 1064 nm to be attributed to the use of a reduced laser emission power at this wavelength, as already mentioned above.

5.2 Case Study on 02 October 2012

A second flight took place on 2 October 2012. During the ascending spiral, in-situ sensors on board the ATR42 were operated in the altitude region from 680 m to 5700 m, covering the 44 min time interval between 19.43 and 20.27 UTC.

230 BASIL was operated over the time interval time interval 16.00-24.00 UTC.

Wind direction measurements performed by the on-board flight sensors reveal a North-Westerly wind, with direction varying in the range 220-320° depending on altitude. Figure 11 shows the 5-days back-trajectories from the NOAA HYSPLIT model at 600 m, 4000 m and 6000 m (in red, blue and green, respectively), ending on the lidar site at 20.00 UTC on 2 October 2012. HYSPLIT back-trajectories confirm the in situ data in terms of wind direction.

235 These results reveal that air masses reaching the measurement site at an altitude of 600 m were originated in Northern Atlantic Ocean, south of Iceland, and passed at low altitudes (500-600 m) over continental areas with high anthropic impact (Ireland, England and Northern France). A different path characterizes air masses at 4000 m. These originated over the Northern Atlantic Sea, off-shore the Canadian coast, and overpassed the Northern coast of Spain before reaching the measurement site. Finally, the air masses reaching the measurement site at 6000 m originated over the North Pacific Ocean,

240 overpassed Canada, the North Atlantic Ocean, the northern coast of Spain and finally reached the measurement site.

In the analysis of this second case study, we applied a different approach: we didn't formulate any a-priori hypothesis on the composition of the sounded aerosol particles. The aerosol typology was instead determined by minimizing variances between measured and simulated particle backscattering profiles at 355 nm and 532 nm. Initial values in terms of modal radius, $\bar{r}$, standard deviation, σ, and refractive index for the different aerosol components were taken from d'Almeida et al.

245 (1991). At each altitude, the particle size distribution measured by the optical particle counter is compared with the five aerosol typologies listed in d'Almeida et al. (1991), which for the sake of clarity are reproduced below:

• Average continental (continental environment influenced by anthropic pollution),

• Urban (continental environment heavy influenced by anthropic pollution),

• Maritime-polluted (environment polluted as Mediterranean Sea or Northern Atlantic),

250   • Clean-polar (Artic environment during summer period),

• Clean continental-rural (rural continental environment without pollution).

Specifically, both urban and continental aerosols include a soot and pollution fine mode component (as both aerosol types include the same aerosol components, they are treated together as a single aerosol type in what follows), a water soluble accumulation mode component and dust-like coarse mode component; the maritime polluted aerosol type includes a soot and

255   pollution fine mode component, a water soluble accumulation mode component and sea-salt coarse mode component; the summer-time Artic aerosol type includes a sulphate fine mode component and a sea salt and mineral accumulation mode component; the rural aerosol type includes a water soluble accumulation mode component and dust-like coarse mode component. As for the previous case study, given the microphysical parameters and aerosol typology for each of the three given modes, the number of particles has been varied in order to have the theoretical distribution matching the experimental

260   distribution computed with the OPC data, with the matching between the experimental and theoretical distributions once again based on a best fit procedure.

The modal radius, standard deviation and refractive index reported by d'Almeida et al. (1991) for the different considered aerosol components are listed in Table 2.

Figure 12 illustrates the vertical profiles of measured (black line) and simulated particle backscattering coefficient at 355 nm

265   over the 44 min time interval between 19.43 and 20.27 UTC on 02 October 2012. Simulated particle backscatter profiles include all five aerosol components specified above, i.e. the Continental/Urban components (red dashed line), the Continental (rural) component (green dashed-dotted line), the Arctic Summer component (black dashed line) and the Marine (polluted) component (blue dashed-dotted line).

Figure 12 reveals a good agreement between the measured backscattering coefficient profile at 355 nm and those simulated

270   at this same wavelength assuming a Continental/Urban aerosol component and a Marine (polluted) aerosol component. We applied this same analysis approach also to the data at 532 nm, with figure 13 illustrating the vertical profiles of measured and simulated particle backscattering coefficient at 532 nm over the same time interval considered in figure 12. Again, simulated particle backscatter profiles include the five above specified aerosol components.

Figure 13 reveals that the measured particle backscattering coefficient profile at 532 nm is well reproduced by the simulated

275   profiles at this same wavelength, especially those obtained considering a Continental/Urban aerosol component and a Marine (polluted) aerosol component, with simulated profiles slightly underestimating the measured profile, but being within or slightly outside the measurement error bar. Deviations between measured and simulated profiles are larger within the aerosol layers centred at 3000m and 4000 m.

More specifically, in this case study, differently from the first one, a modified version of the approach defined by Di Iorio et

280   al. (2003) was applied in order to determine the sounded aerosol typology. This approach is based on the minimization of the relative deviation between the measured and the simulated particle backscattering coefficient, i.e.:

$$\Delta = \frac{1}{N_p} \sum_{k=1}^{N_p} \frac{|\beta_{\lambda(simulated)}(z_k) - \beta_{k(measured)}(z_k)|}{\beta_{\lambda(measured)}(z_k)}, \tag{8}$$

Atmospheric
Measurement
Techniques
Discussions

where z_k is the altitude. Figure 14 illustrates the deviations between the measured and the simulated particle backscattering coefficient profiles at 355 nm.

285   The smallest deviations between measured and simulated particle backscattering coefficient profiles over the considered altitude range are obtained when considering the presence of a Continental/Urban aerosol component (not exceeding 15 % up to 5000 m, with a mean deviation of 5.9 %). Deviations between measured and simulated profiles obtained considering a Marine polluted aerosol component are slightly exceeding these (smaller than 20 % up to 5000 m, with a mean deviation of 9.5 %), while simulated profile obtained considering the presence of either a Continental rural or an Arctic Summer aerosol

290   component largely deviate from the measured profile (up to 80 %, with a mean deviation of 50.9% and 25.9%, respectively). Figure 15 illustrates the deviations between measured and simulated particle backscattering coefficient profiles at 532 nm. Again, the smallest deviations between the measured and simulated profiles are obtained over the considered altitude range are obtained when considering a Continental/Urban aerosol component (not exceeding 50 % up to 5000 m, with a mean deviation of 25.9 %), with the only exception for the interval 3100-3700 m, where simulated profile obtained considering a

295   Marine polluted aerosol component deviate less. Above 3700 m simulated profiles obtained considering Continental/Urban and Marine polluted aerosol component equally deviate from the measured profile.

In the attempt to simultaneously minimize deviations between measured and simulated particle backscattering profiles at both 355 and 532 nm, a total deviation can be computed as the root sum square of the single deviations at the two wavelengths, which can be expressed as:

300
$$\Delta_{tot} = \sqrt{\Delta_{355}^2 + \Delta_{532}^2}, \qquad\qquad (9)$$

This quantity was calculated for the five distinct aerosol components. Figure 16 illustrates the total deviations between the measured and the simulated particle backscattering coefficient profiles at 355 and 532 nm for the different aerosol components.

In order to facilitate the interpretation of these results, the total deviation between measured and simulated particle

305   backscattering coefficient profiles for the different aerosol components has been plotted together with the measured particle backscattering profiles at both 355 and 532 nm (figure 17). It is to be noticed that the deviation in the form of the particle backscattering profiles at 355 and 532 nm below 600 m is due to the overlap effect, which is primarily affecting the inversion procedure applied to the 532 nm elastic signals in this altitude interval. The inversion approach applied to the elastic signals to determine the corresponding particle backscattering coefficient profiles is in fact different for the two

310   wavelengths (355 and 532 nm). Specifically, particle backscattering coefficient profiles at 355 nm are obtained through the application of the Raman techniques, which relies on the ratio between the 355 nm elastic signal and the simultaneous molecular nitrogen roto-vibrational Raman signal; these two signals are characterized by an almost identical overlap function, and therefore the overlap effect cancel out when ratioing the signals. As opposed to this, particle backscattering coefficient profiles at 532 nm are obtained through the application of a Klett-modified inversion approach (Di Girolamo *et*

315   *al.*, 1995, 1999), which does not rely on the ratio between signals with an almost identical overlap function.

Atmospheric
Measurement
Techniques
Discussions

Figure 17 allows revealing the following considerations. In the lowest portion of the atmosphere, up to an altitude of ~1300 m (altitude 1), aerosol particles are most likely characterized by a predominant Continental/Urban component. This aerosol layer extends up to ~1600 m, which is the altitude where the boundary layer height is located as also indicated by the simultaneous radiosonde data (not shown here). In the upper portion of the boundary layer, in the vertical interval 1300-1600

320   m, deviations associated with Continental/Urban, Marine polluted and Continental rural component overlap, which suggests that all three aerosol components are possible. However, while this upper portion of the boundary layer is typically characterized by entrainment effects (interfacial region), which may allow different aerosol components to be ingested, the Continental/Urban component is likely to be the predominant component.

Above the top of the boundary layer and up to ~2700 m (altitude 2), particle backscatter decreases with altitude, which is

325   probably the effect of the decreasing number concentration of the same aerosol type (Continental/Urban) as a results of the progressive attenuation of the underlying convective activity. The typology analysis suggests Continental/Urban aerosols likely to be the predominant component, as in fact total deviation between the measured and the simulated particle backscattering coefficient profiles for this aerosol component is far lower than for all other aerosol components.

In the altitude interval 2700-3600 m (altitudes 2-3, with max. at 3000 m) the measured particle backscatter profiles reveal the

330   presence of a distinct aerosol layer. The typology analysis indicates both the Continental/Urban and the Marine polluted components to be possible. An additional distinct aerosol layer is found in the altitude interval 3600-4600 m (altitudes 3-4, with max. at 4000 m). Again, the typology analysis suggests both the Continental/Urban and the Marine polluted components to be possible. Sounded aerosol particles at 3000 and 4000 m are compatible with an internal mixture of continental polluted aerosols with marine salt (i.e. an aerosols originated in a marine environment and mixed with polluted

335   continental aerosols), this possibility being confirmed by the back-trajectory analysis at 3000 and 4000 m.

6 Summary

During HyMeX-SOP1, the Raman lidar system BASIL was deployed in Candillargues (Southern France) and operated almost continuously over a two month period in the time frame October-November 2012. Dedicated flights of the French research aircraft ATR42 were carried out in the frame of the EUFAR-WaLiTemp Project. The ATR42 payload included *in*

340   *situ* sensors for turbulence measurements, as well as aerosol/cloud microphysics probes. Among these, an optical particle counter (GRIMM Aerosol Technik GmbH, model: Sky-OPC 1.129) capable of measuring particle number concentration in the size interval 0.25 - 2.5 μm. A specific flight pattern was considered for the purpose of this study, with the aircraft making spirals up and down around a central location approximately 20 km eastward of the lidar site. Vertical profiles of the particle backscattering coefficient at 355, 532 and 1064 nm have been simulated through the use of a Mie scattering code, using the

345   data provided by the optical particle counter. The simulated particle backscatter profiles have been compared with the profiles measured by the lidar Raman system BASIL. Results from two selected case studies (on 13 September and on 02 October 2012) were reported and discussed. Two slightly different analysis approaches, both based on the application of a

Atmospheric
Measurement
Techniques

Open Access

EGU

Discussions

Mie scattering code, are considered and applied. These approaches ultimately allow inferring the sounded aerosol type and its primary microphysical properties.

350 The HYSPLIT-NOAA back-trajectory model was used to verify the origin of the sounded aerosol particles. In the approach applied to the first case study an hypothesis on aerosol composition is formulated in the light of the involved air masses and their back-trajectories. Simulations of the particle backscattering coefficient profile are carried based on an assumed aerosol composition. In this approach, literature values of the modal radius, standard deviation and refractive index for the different aerosol components of the assumed aerosol typologies are used as input parameters for the simulations. In

355 order to quantify the agreement between measured and simulated particle backscattering profiles at the three wavelengths, the root mean squared (RMS) deviation and BIAS are calculated for each profile pair. At 355 nm the BIAS of the measured vs. the simulated profile is in the range $-1.3 \div 6.45$ % up to 3900 m, while RMS deviation is in the range 1.2-7.5 %. Above this altitude both the BIAS and the RMS deviation exceed 25 %. At 532 nm the BIAS is in the range ±10 % up to 3000 m and the RMS deviation is not exceeding 15 %. At 1064 nm BIAS and RMS deviation are rather large, with values within ±

360 30 % up to 2500 m. The small BIAS and RMS deviation values, especially at 355 and 532 nm, demonstrate the applicability of the considered approach to infer sounded aerosol typologies.

In the second approach, which is been applied to second case study, no a-priori hypothesis concerning aerosol composition is formulated and five different aerosol typologies (Continental polluted, Clean continental-rural, Urban, Maritime-polluted and Clean-polar) are considered, with their size and microphysical properties taken from literature. The approach leads to an

365 assessment of predominant aerosol component based on the application of a minimization approach applied to the deviations between measured and the simulated particle backscattering profiles at 355 and 532 nm, considering all five aerosol typologies. The application of this approach suggests that Continental/Urban aerosols are likely to be the predominant component up to ~1600 m, while two distinct aerosol layers located in the altitude regions 2700-3600 m (with max. at 3000 m) and 3600-4600 m (with max. at 4000 m) are identified through the typology analysis to likely consists of

370 Continental/Urban and/or Marine polluted aerosols, respectively. The two aerosol layers are also compatible with an internal mixture of continental polluted aerosol particles with marine salt (i.e. marine aerosols mixed with polluted continental aerosols), this possibility having been verified through back-trajectory analysis.

Atmospheric
Measurement
Techniques
Discussions

References

Ansmann, A., Riebesell, M. and Weitkamp, C.: Measurement of atmospheric aerosol extinction profiles with a Raman lidar,
380 Opt. Lett., OL, 15(13), 746–748, doi:10.1364/OL.15.000746, 1990.

Ansmann, A., Wandinger, U., Riebesell, M., Weitkamp, C. and Michaelis, W.: Independent measurement of extinction and
backscatter profiles in cirrus clouds by using a combined Raman elastic-backscatter lidar, Appl. Opt., AO, 31(33), 7113–
7131, doi:10.1364/AO.31.007113, 1992.

Behrendt, A., Wulfmeyer, V., Bauer, H.-S., Schaberl, T., Di Girolamo, P., Summa, D., Kiemle, C., Ehret, G., Whiteman, D.
385 N., Demoz, B. B., Browell, E. V., Ismail, S., Ferrare, R., Kooi, S. and Wang, J.: Intercomparison of Water Vapor Data
Measured with Lidar during IHOP_2002. Part I: Airborne to Ground-Based Lidar Systems and Comparisons with Chilled-
Mirror Hygrometer Radiosondes, J. Atmos. Oceanic Technol., 24(1), 3–21, doi:10.1175/JTECH1924.1, 2007.

Bhawar, R., Di Girolamo, P., Summa, D., Flamant, C., Althausen, D., Behrendt, A., Kiemle, C., Bosser, P., Cacciani, M.,
Champollion, C., Di Iorio, T., Engelmann, R., Herold, C., Müller, D., Pal, S., Wirth, M. and Wulfmeyer, V.: The water
390 vapour intercomparison effort in the framework of the Convective and Orographically-induced Precipitation Study: airborne-
to-ground-based and airborne-to-airborne lidar systems, Quarterly Journal of the Royal Meteorological Society, 137(S1),
325–348, doi:10.1002/qj.697, 2011.

d'Almeida, G. A., Koepke, P. and Shettle E. P.: Atmospheric aerosols: Global climatology and radiative characteristics, A
Deepak Publishing, Hampton, Virginia, 561 pp., 1991.

395 Di Girolamo, P., Gagliardi, R. V., Pappalardo, G., Spinelli, N., Velotta, R. and Berardi, V.: Two wavelength lidar analysis of
stratospheric aerosol size distribution, Journal of Aerosol Science, 26(6), 989–1001, doi:10.1016/0021-8502(95)00025-8,
1995.

Di Girolamo, P., Ambrico, P. F., Amodeo, A., Boselli, A., Pappalardo, G. and Spinelli, N.: Aerosol observations by lidar in
the nocturnal boundary layer, Appl. Opt., AO, 38(21), 4585–4595, doi:10.1364/AO.38.004585, 1999.

400 Di Girolamo, P., Marchese, R., Whiteman, D. N. and Demoz, B. B.: Rotational Raman Lidar measurements of atmospheric
temperature in the UV, Geophysical Research Letters, 31(1), doi:10.1029/2003GL018342, 2004.

Di Girolamo, P., Behrendt, A. and Wulfmeyer, V.: Spaceborne profiling of atmospheric temperature and particle extinction
with pure rotational Raman lidar and of relative humidity in combination with differential absorption lidar: performance
simulations, Appl. Opt., AO, 45(11), 2474–2494, doi:10.1364/AO.45.002474, 2006.

405 Di Girolamo, P., Behrendt, A., Kiemle, C., Wulfmeyer, V., Bauer, H., Summa, D., Dörnbrack, A. and Ehret, G.: Simulation
of satellite water vapour lidar measurements: Performance assessment under real atmospheric conditions, Remote Sensing of
Environment, 112(4), 1552–1568, doi:10.1016/j.rse.2007.08.008, 2008.

Di Girolamo, P., Summa, D. and Ferretti, R.: Multiparameter Raman Lidar Measurements for the Characterization of a Dry
Stratospheric Intrusion Event, J. Atmos. Oceanic Technol., 26(9), 1742–1762, doi:10.1175/2009JTECHA1253.1, 2009a.

Atmospheric
Measurement
Techniques
Discussions

410   Di Girolamo, P., Summa, D., Lin, R.-F., Maestri, T., Rizzi, R. and Masiello, G.: UV Raman lidar measurements of relative humidity for the characterization of cirrus cloud microphysical properties, Atmos. Chem. Phys., 9(22), 8799–8811, doi:10.5194/acp-9-8799-2009, 2009b.

Di Girolamo, P., Summa, D., Bhawar, R., Di Iorio, T., Cacciani, M., Veselovskii, I., Dubovik, O. and Kolgotin, A.: Raman lidar observations of a Saharan dust outbreak event: Characterization of the dust optical properties and determination of

415   particle size and microphysical parameters, Atmospheric Environment, 50, 66–78, doi:10.1016/j.atmosenv.2011.12.061, 2012a.

Di Girolamo, P., Summa, D., Cacciani, M., Norton, E. G., Peters, G. and Dufournet, Y.: Lidar and radar measurements of the melting layer: observations of dark and bright band phenomena, Atmospheric Chemistry and Physics, 12(9), 4143–4157, doi:https://doi.org/10.5194/acp-12-4143-2012, 2012b.

420   Di Girolamo, P., Flamant, C., Cacciani, M., Richard, E., Ducrocq, V., Summa, D., Stelitano, D., Fourrié, N. and Saïd, F.: Observation of low-level wind reversals in the Gulf of Lion area and their impact on the water vapour variability, Quarterly Journal of the Royal Meteorological Society, 142(S1), 153–172, doi:10.1002/qj.2767, 2016.

Di Girolamo, P., Cacciani, M., Summa, D., Scoccione, A., De Rosa, B., Behrendt, A. and Wulfmeyer, V.: Characterisation of boundary layer turbulent processes by the Raman lidar BASIL in the frame of HD(CP)2 Observational Prototype

425   Experiment, Atmospheric Chemistry and Physics, 17(1), 745–767, doi:https://doi.org/10.5194/acp-17-745-2017, 2017.

Di Girolamo, P., Behrendt, A. and Wulfmeyer, V.: Space-borne profiling of atmospheric thermodynamic variables with Raman lidar: performance simulations, Opt. Express, OE, 26(7), 8125–8161, doi:10.1364/OE.26.008125, 2018a.

Di Girolamo, P., Scoccione, A., Cacciani, M., Summa, D., De Rosa, B. and Schween, J. H.: Clear-air lidar dark band, Atmospheric Chemistry and Physics, 18(7), 4885–4896, doi:https://doi.org/10.5194/acp-18-4885-2018, 2018b.

430   Di Iorio, T., Di Sarra, A., Junkermann, W., Cacciani, M., Fiocco, G. and Fuà, D.: Tropospheric aerosols in the Mediterranean: 1. Microphysical and optical properties, Journal of Geophysical Research: Atmospheres, 108(D10), doi:10.1029/2002JD002815, 2003.

Draxler, R. R and Hess, G. D.: An overview of the HYSPLIT_4 modeling system for trajectories, dispersion and deposition. Australian meteorological magazine, 47(4), 295–308, 1998.

435   Elterman, L.: Aerosol Measurements in the Troposphere and Stratosphere, Appl. Opt., AO, 5(11), 1769–1776, doi:10.1364/AO.5.001769, 1966.

Fernald, F. G.: Analysis of atmospheric lidar observations: some comments, Appl. Opt., AO, 23(5), 652–653, doi:10.1364/AO.23.000652, 1984.

Fiocco, G. and Grams, G.: Observations of the Aerosol Layer at 20 km by Optical Radar, J. Atmos. Sci., 21(3), 323–324,

440   doi:10.1175/1520-0469(1964)021<0323:OOTALA>2.0.CO;2, 1964.

Grimm, H. and Eatough, D. J.: Aerosol Measurement: The Use of Optical Light Scattering for the Determination of Particulate Size Distribution, and Particulate Mass, Including the Semi-Volatile Fraction, Journal of the Air & Waste Management Association, 59(1), 101–107, doi:10.3155/1047-3289.59.1.101, 2009.

Atmospheric
Measurement
Techniques
Open Access
Discussions
EGU

Haywood, J. and Boucher, O.: Estimates of the direct and indirect radiative forcing due to tropospheric aerosols: A review,
445   Reviews of Geophysics, 38(4), 513–543, doi:10.1029/1999RG000078, 2000.

Heim, M., Mullins, B. J., Umhauer, H. and Kasper, G.: Performance evaluation of three optical particle counters with an efficient "multimodal" calibration method, Journal of Aerosol Science, 39(12), 1019–1031, doi:10.1016/j.jaerosci.2008.07.006, 2008.

Junge, C. and Jaenicke, R.: New results in background aerosols studies from the Atlantic expedition of the R.V. Meteor,
450   Spring 1969, Journal of Aerosol Science, 2(3), 305–314, doi:10.1016/0021-8502(71)90055-3, 1971.

Junge, C. E.: Our knowledge of the physico-chemistry of aerosols in the undisturbed marine environment, Journal of Geophysical Research, 77(27), 5183–5200, doi:10.1029/JC077i027p05183, 2012.

Klett, J. D.: Stable analytical inversion solution for processing lidar returns, Appl. Opt., AO, 20(2), 211–220, doi:10.1364/AO.20.000211, 1981.

455   Klett, J. D.: Lidar inversion with variable backscatter/extinction ratios, Appl. Opt., AO, 24(11), 1638–1643, doi:10.1364/AO.24.001638, 1985.

McMeeking, G. R., Hamburger, T., Liu, D., Flynn, M., Morgan, W. T., Northway, M., Highwood, E. J., Krejci, R., Allan, J. D., Minikin, A. and Coe, H.: Black carbon measurements in the boundary layer over western and northern Europe, Atmos. Chem. Phys., 10(19), 9393–9414, doi:10.5194/acp-10-9393-2010, 2010.

460   Mitchell, J. M.: The Effect of Atmospheric Aerosols on Climate with Special Reference to Temperature near the Earth's Surface, J. Appl. Meteor., 10(4), 703–714, doi:10.1175/1520-0450(1971)010<0703:TEOAAO>2.0.CO;2, 1971.

Müller, D., Wandinger, U., Althausen, D. and Fiebig, M.: Comprehensive particle characterization from three-wavelength Raman-lidar observations: case study, Appl. Opt., AO, 40(27), 4863–4869, doi:10.1364/AO.40.004863, 2001.

Müller D., Mattis, I., Ansmann, A., Wandinger, U., Ritter, C. and Kaiser, D.: Multiwavelength Raman lidar observations of
465   particle growth during long-range transport of forest-fire smoke in the free troposphere, Geophysical Research Letters, 34(5), doi:10.1029/2006GL027936, 2007.

Müller, T., Schladitz, A., Massling, A., Kaaden, N., Kandler, K. and Wiedensohler, A.: Spectral absorption coefficients and imaginary parts of refractive indices of Saharan dust during SAMUM-1, Tellus B: Chemical and Physical Meteorology, 61(1), 79–95, doi:10.1111/j.1600-0889.2008.00399.x, 2009.

470   Sekiguchi, M., Nakajima, T., Suzuki, K., Kawamoto, K., Higurashi, A., Rosenfeld, D., Sano, I. and Mukai, S.: A study of the direct and indirect effects of aerosols using global satellite data sets of aerosol and cloud parameters, Journal of Geophysical Research: Atmospheres, 108(D22), doi:10.1029/2002JD003359, 2003.

Stein, A. F., Draxler, R. R., Rolph, G. D., Stunder, B. J. B., Cohen, M. D. and Ngan, F.: NOAA's HYSPLIT Atmospheric Transport and Dispersion Modeling System, Bull. Amer. Meteor. Soc., 96(12), 2059–2077, doi:10.1175/BAMS-D-14-
475   00110.1, 2015.

Takemura, T., Nozawa, T., Emori, S., Nakajima, T.Y. and Nakajima, T.: Simulation of climate response to aerosol direct and indirect effects with aerosol transport-radiation model, Journal of Geophysical Research: Atmospheres, 110(D2), doi:10.1029/2004JD005029, 2005.

Veselovskii, I., Kolgotin, A., Griaznov, V., Müller, D., Wandinger, U. and Whiteman, D. N.: Inversion with regularization
480   for the retrieval of tropospheric aerosol parameters from multiwavelength lidar sounding, Appl. Opt., AO, 41(18), 3685–3699, doi:10.1364/AO.41.003685, 2002.

Veselovskii, I., Whiteman, D. N., Kolgotin, A., Andrews, E. and Korenskii, M.: Demonstration of Aerosol Property Profiling by Multiwavelength Lidar under Varying Relative Humidity Conditions, J. Atmos. Oceanic Technol., 26(8), 1543–1557, doi:10.1175/2009JTECHA1254.1, 2009.

485   Veselovskii, I., Dubovik, O., Kolgotin, A., Lapyonok, T., Di Girolamo, P., Summa, D., Whiteman, D. N., Mishchenko, M. and Tanré, D.: Application of randomly oriented spheroids for retrieval of dust particle parameters from multiwavelength lidar measurements, Journal of Geophysical Research: Atmospheres, 115(D21), doi:10.1029/2010JD014139, 2010.

WCP-112, A Preliminary Cloudless Standard Atmosphere for Radiation Computation. WCP/IAMAP Radiation Commission. Geneva: WCP, (ICSU /WMO/WCP/IAMAP) (WCP-112). ii, 53 p. Call no: WCP 112 TD 241986, 1986.

490   Wulfmeyer, V., Bauer, H., Di Girolamo, P. and Serio, C.: Comparison of active and passive water vapor remote sensing from space: An analysis based on the simulated performance of IASI and space borne differential absorption lidar, Remote Sensing of Environment, 95(2), 211–230, doi:10.1016/j.rse.2004.12.019, 2005.

Yang, F., Tan, J., Zhao, Q., Du, Z., He, K., Ma, Y., Duan, F., Chen, G. and Zhao, Q.: Characteristics of PM2.5 speciation in representative megacities and across China, Atmos. Chem. Phys., 11(11), 5207–5219, doi:10.5194/acp-11-5207-2011, 2011.

495

16
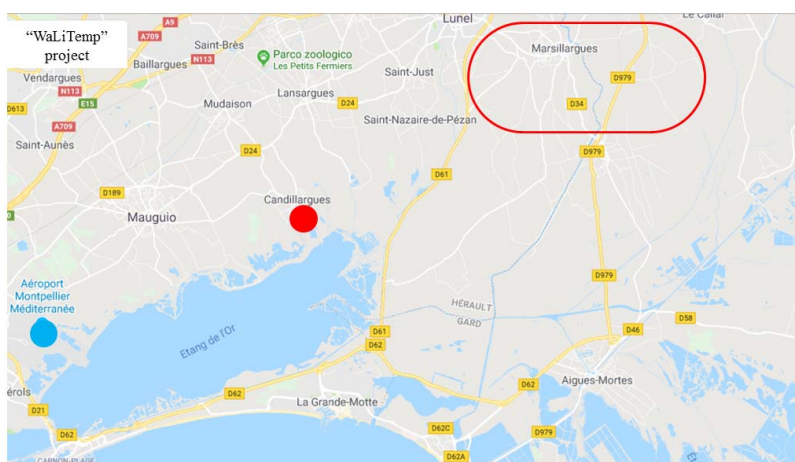
500 **Figure 1: ATR42 flight pattern in the frame of the "WaLiTemp" project (red line). The light blue dot represents the position of Montpellier Airport, where the ATR-42 was taking-off and landing, while the red dot represent the position of the Raman lidar BASIL. The red curve represents the footprint of the aircraft pattern. The distance between the lidar site and the flight pattern is approx. 20 km.**
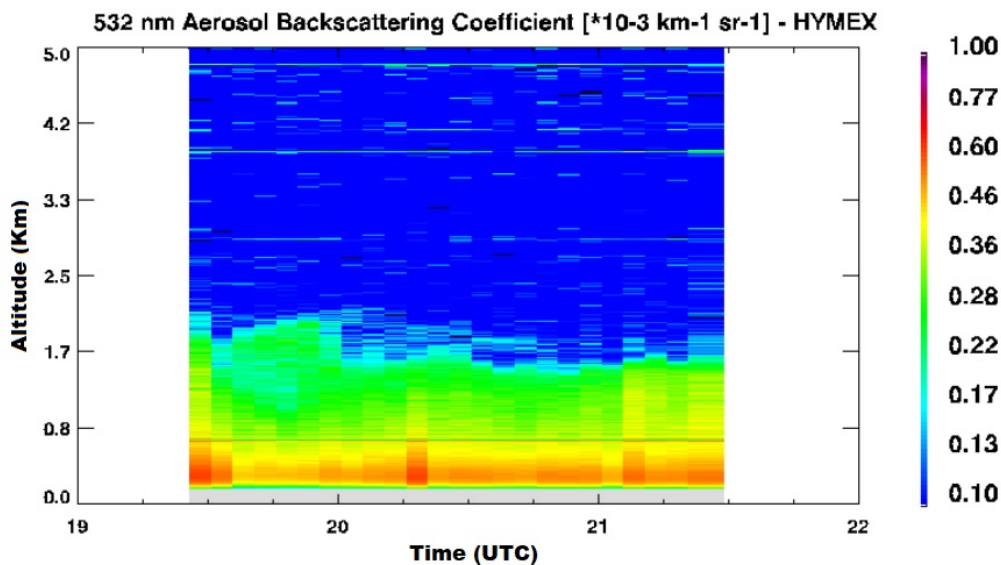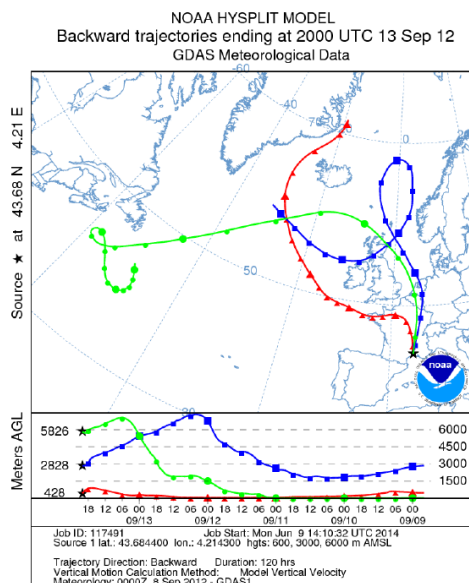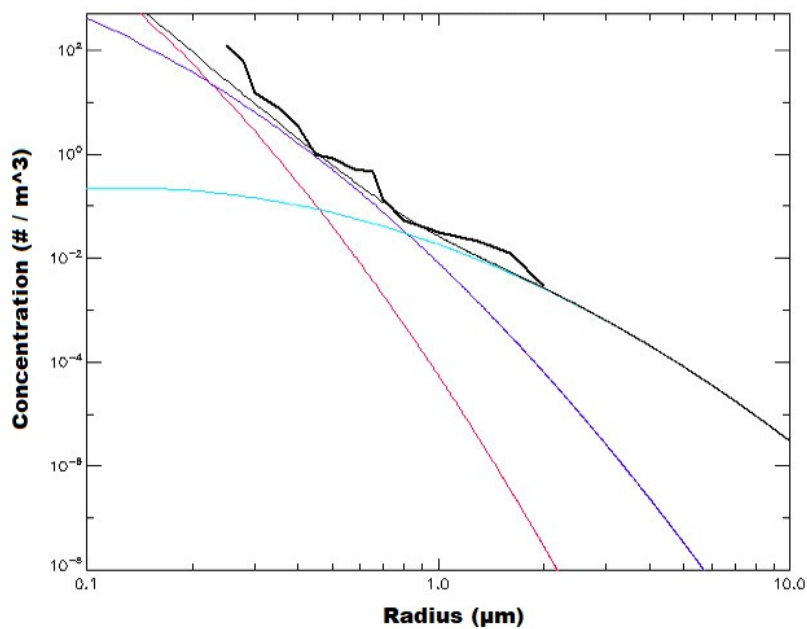

Figure 2: Time evolution of the particle backscattering coefficient at 532 nm over the time interval 19.30-21.30 UTC on 13 September 2012.

505

Figure 3: Air masses back-trajectories at 428 m (red), 2828 m (blue) and 5826 m (green) ending over the lidar site at 20 UTC on 13 September 2012.

18

**Figure 4: Size distribution computed from the OPC data (bold black line), together with the total theoretical distribution (thin
510   black line) and theoretical distributions for the three different modes: fine mode (soot and pollution, red line), accumulation mode
(water-soluble aerosols, violet line) and coarse mode (sea salt, light blue line).**

Wavelengths/Component	Soot (fine mode)		water-soluble (accumulation mode)		sea salt (coarse mode)	
	n_r	n_i	n_r	n_i	n_r	n_i
350nm	1.750	0.465	1.530	$5.00E^{-3}$	1.390	$1.20E^{-7}$
550nm	1.750	0.440	1.530	$6.00E^{-3}$	1.381	$3.70E^{-9}$
1000nm	1.760	0.440	1.520	$1.55E^{-2}$	1.370	$2.43E^{-5}$

Table 1: Values of n_r and n_i at 350, 550 and 1000 nm for the three different aerosol components.

19
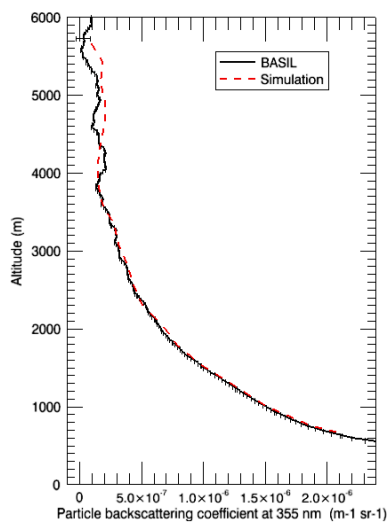
Figure 5: Vertical profiles of the measured (black line) and simulated (red line) particle backscattering coefficient at 355 nm over the time interval 19.55-20.35 UTC on 13 September 2012. The error bar in lidar measurements accounts for the statistical uncertainty.
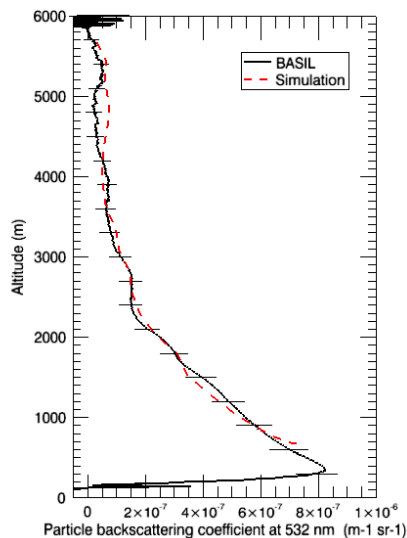
Figure 6: Same as Fig. 5 but for the particle backscattering coefficient at 532 nm.
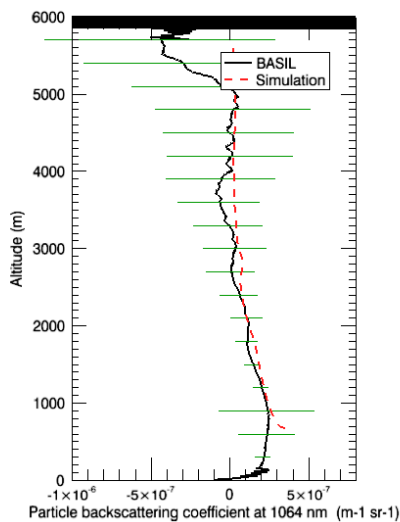
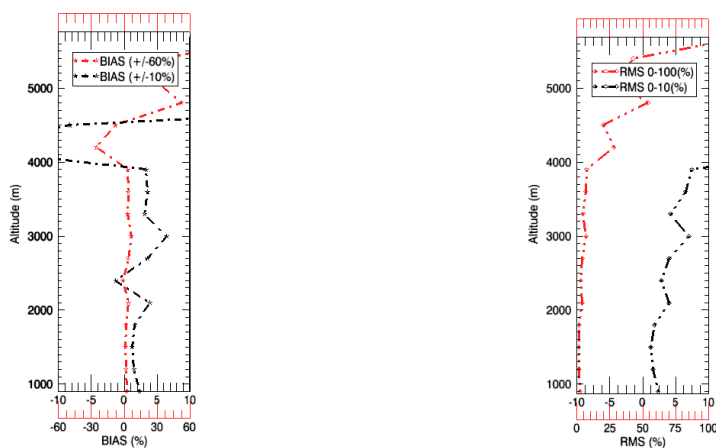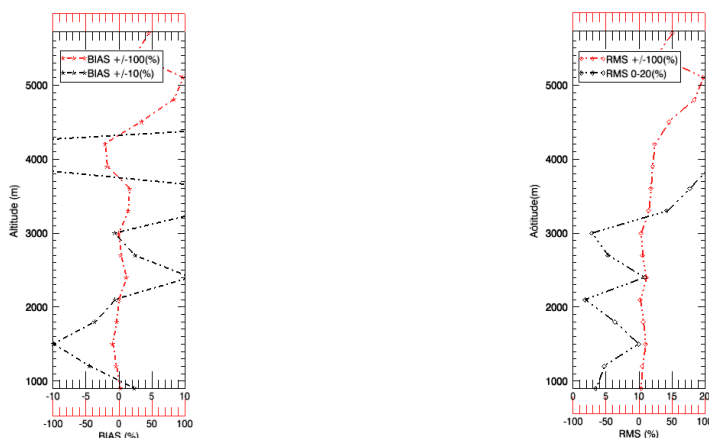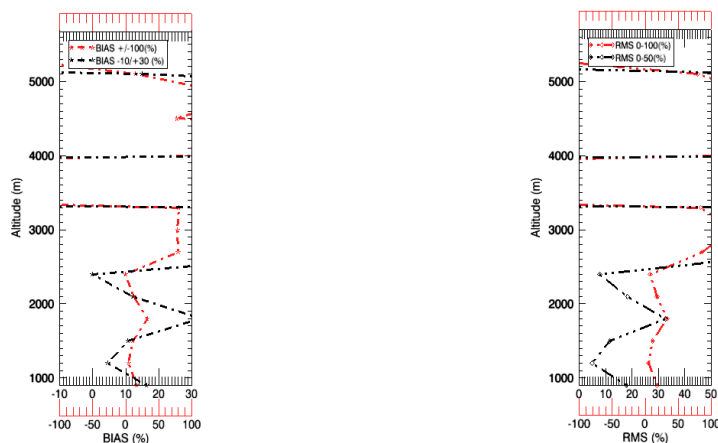**Figure 7: Same as Fig. 5 but for the particle backscattering coefficient at 1064 nm**


Figure 8: Vertical profiles of the BIAS (left panel) and RMS deviation (right panel), expressed in percentage, of the measured vs. the simulated particle backscattering coefficient at 355 nm. Black and red lines represent two different variability ranges (± 10 % and ± 60 %, respectively, for the BIAS, and 0-10 % and 0-100 %, respectively, for the RMS deviation).

Atmospheric
Measurement
Techniques

Open Access

Discussions

525

Figure 9: Vertical profiles of BIAS (left panel) and RMS deviation (right panel), expressed in percentage, of the measured vs. the simulated particle backscattering coefficient at 532 nm. Black and red lines represent two different variability ranges (± 10 % and ± 100 %, respectively, for the BIAS, and 0-10 % and 0-100 %, respectively, for the RMS deviation.

530   **Figure 10: Vertical profiles of BIAS (left panel) and RMS deviation (right panel), expressed in percentage, of the measured vs. the simulated particle backscattering coefficient at 1064 nm. Black and red lines represent two different variability ranges (± 10 % and ± 100 %, respectively, for the BIAS, and 0-50 % and 0-100 %, respectively, for the RMS deviation**

Atmospheric
Measurement
Techniques
Discussions

Open Access
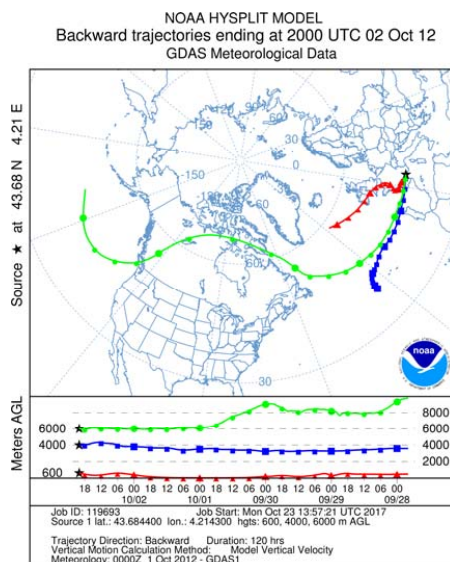
Figure 11: Back-trajectories at 600 m (red), 4000 m (blue) and 6000 m (green) ending on the lidar site at 20 UTC on 02 October 2012.

535

	$\bar{r}$ (µm)	σ	m_r (355 nm)	m_i (355 nm)	m_r (532 nm)	m_i (532 nm)
Soot	0.012	2.00	1.75	4.65×10^{-1}	1.75	4.44×10^{-1}
Water soluble	0.024	2.24	1.53	5.00×10^{-3}	1.53	6.00×10^{-3}
Dust-like	0.471	2.51	1.53	8.00×10^{-3}	1.53	8.00×10^{-3}
Sea-salt (fine)	0.300	2.51	1.39	1.20×10^{-7}	1.38	3.70×10^{-9}
Sulphate	0.069	2.03	1.45	1.00×10^{-8}	1.43	1.00×10^{-8}
Sea-salt (acc.)	0.400	2.03	1.39	1.20×10^{-7}	1.38	3.7×10^{-9}
Mineral	0.270	2.67	1.53	1.70×10^{-2}	1.53	5.50×10^{-3}

Table 2: Modal radius, standard deviation and refractive index (real and imaginary part) for the different considered aerosol components (from d'Almeida *et al*., 1991).
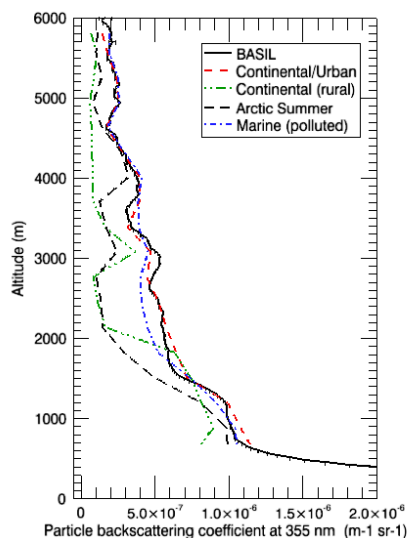
Figure 12: Vertical profiles of measured (black line) and simulated particle backscattering coefficient at 355 nm over the time interval 19.43-20.27 UTC on 02 October 2012. Simulated particle backscatter profiles include five distinct components: Continental/Urban (red dashed line), Continental (rural) (green dashed-dotted line), Arctic Summer (black dashed line) and Marine (polluted) (blue dashed-dotted line). The error bar in lidar measurements accounts for the statistical uncertainty.

540
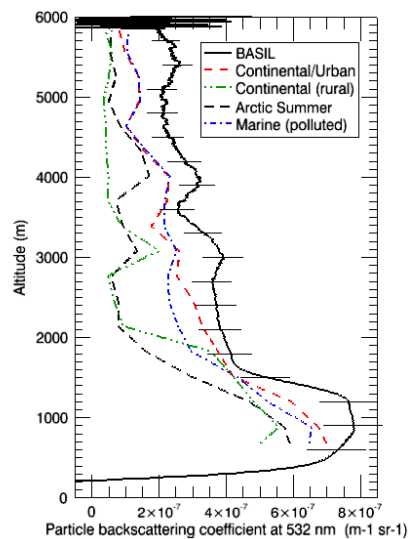
Figure 13: Same as figure 12, but with particle backscattering coefficient profiles at 532 nm.
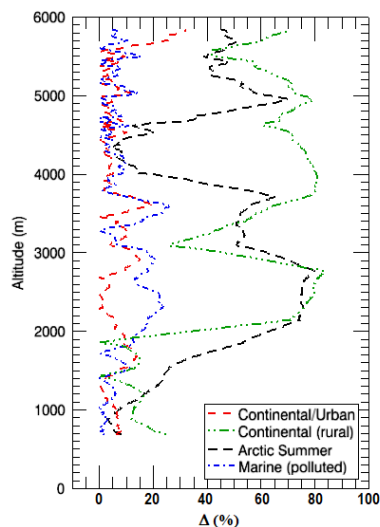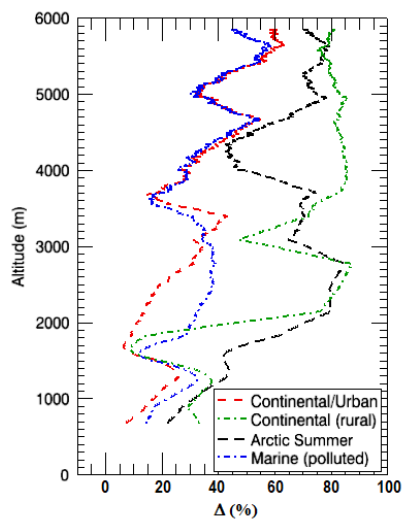
24

545

Figure 14: Deviation, expressed in percentage, between measured and simulated particle backscattering coefficient profiles at 355 nm. Simulated profiles are: Arctic Summer (black dashed line), Continental/Urban (red dashed line), Marine (polluted) (blue dashed-dotted line) and Continental (rural) (green dashed-dotted line).

550

Figure 15: Same as figure 14, but obtained considering particle backscattering coefficient profiles at 532 nm.
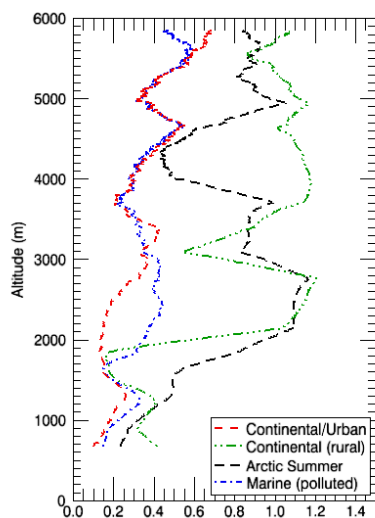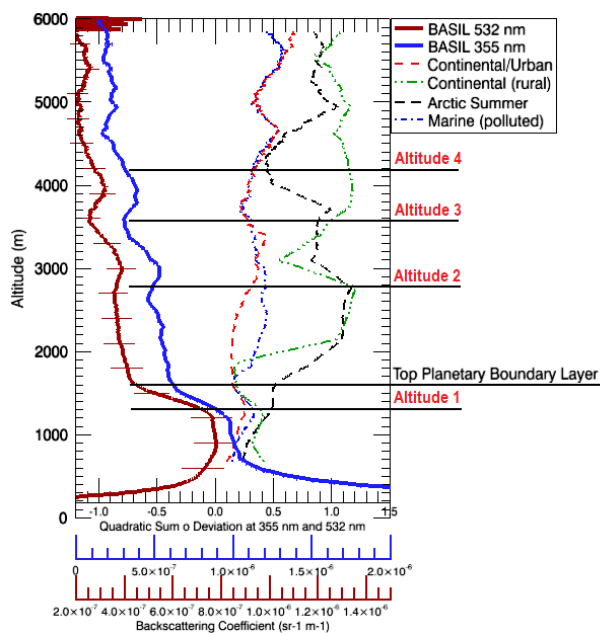
Figure 16: Total deviation between measured and simulated particle backscattering coefficient profiles at 355 and 532 nm for the different aerosol components. Simulated profiles are: Arctic Summer (black dashed line), Continental/Urban (red dashed line),
555 **Marine (polluted) (blue dashed-dotted line) and Continental (rural) (green dashed-dotted line).**

Figure 17: Total deviation between measured and simulated particle backscattering coefficient profiles for the different aerosol components (Arctic Summer: black dashed line, Continental/Urban: red dashed line, Marine polluted: blue dashed-dotted line; Continental rural: green dashed-dotted line) and measured particle backscattering profiles at both 355 (blue line) and 532 nm (red line). The horizontal blue and red axes refer to the particle backscattering coefficient at 355 and 532 nm, respectively, while the horizontal black axis refers to the total deviations. Horizontal black lines are also drawn at specific altitudes to identify different aerosol types in support of the interpretation of the reported results.

560

565